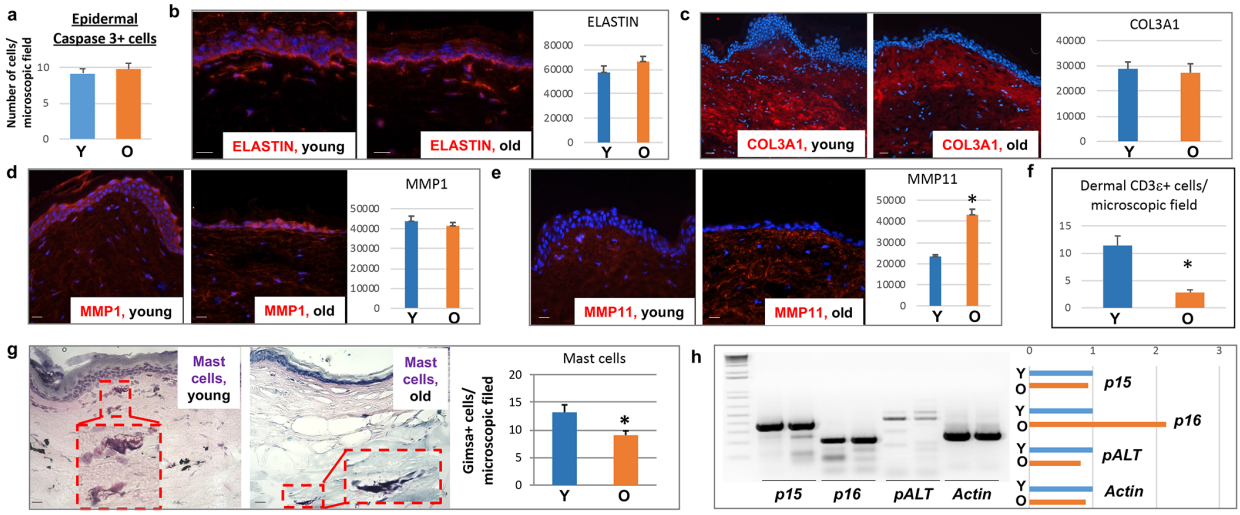

Suppl Figure S1

a

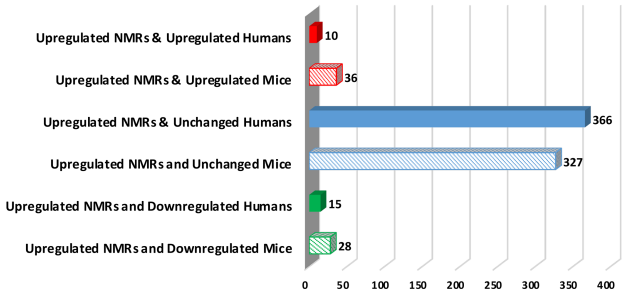
Upregulated NMRs & Upregulated Humans
10
Upregulated NMRs & Upregulated Mice
36
Upregulated NMRs & Unchanged Humans
366
Upregulated NMRs and Unchanged Mice
327
Upregulated NMRs and Downregulated Humans
15
Upregulated NMRs and Downregulated Mice
28
0 50 100 150 200 250 300 350 400

b

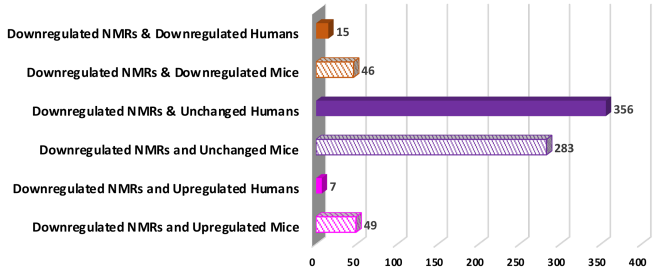
Downregulated NMRs & Downregulated Humans
15
Downregulated NMRs & Downregulated Mice
46
Downregulated NMRs & Unchanged Humans
356
Downregulated NMRs and Unchanged Mice
283
Downregulated NMRs and Upregulated Humans
7
Downregulated NMRs and Upregulated Mice
49
0 50 100 150 200 250 300 350 400

Figure S2

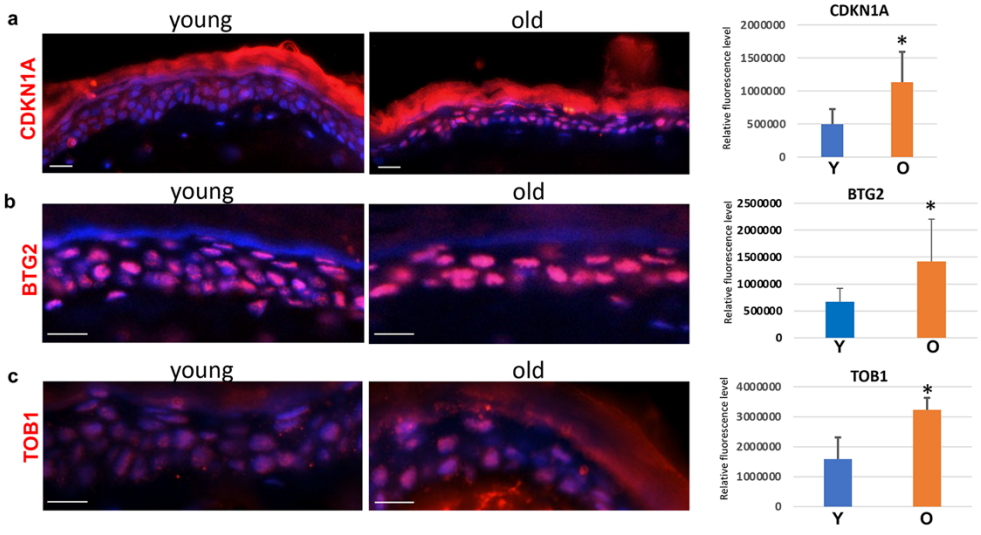

Suppl Figure S3

Genes upregulated in the NMR skin during aging (HAGR database)

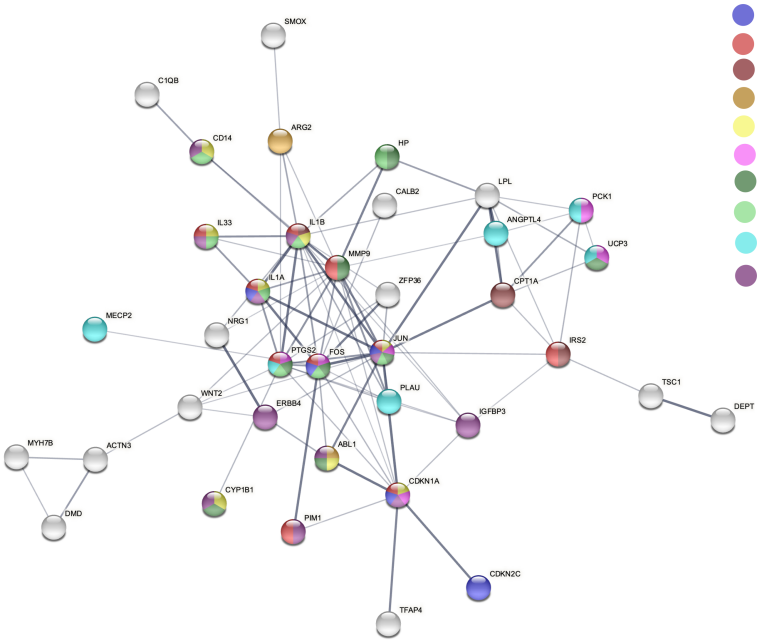

- Senescence-Associated Secretory Phenotype (SASP)
- Cytokine Signaling in Immune system
- Positive regulation of lipid catabolic process
- Regulation of cellular senescence
- Apoptotic signaling pathway
- Aging
- Response to oxidative stress
- Inflammatory response
- Response to hypoxia
- Apoptotic process

Suppl Fig S4

Genes downregulated in the NMR skin during aging (HAGR database)

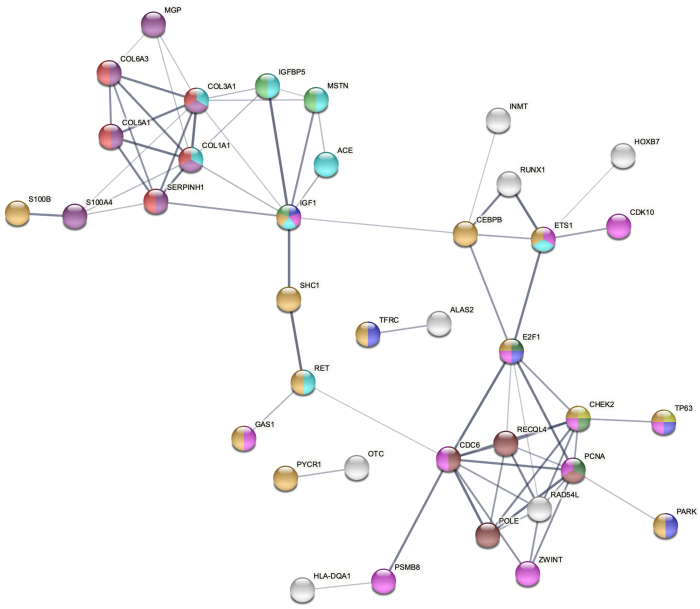

- Regulation of mitochondrion organization
- Collagen biosynthesis and modifying enzymes
- DNA-dependent DNA replication
- Regulation of cell death
- Replicative cell aging
- Regulation of cell cycle
- Regulation of cell cycle g1/s phase transition
- Factors and pathways affecting insulin-like growth factor
- Regulation of cell migration
- Collagen-containing extracellular matrix

Suppl Fig S5

Genes up- and downregulated in the aged NMR skin (CGC and TSG databases)

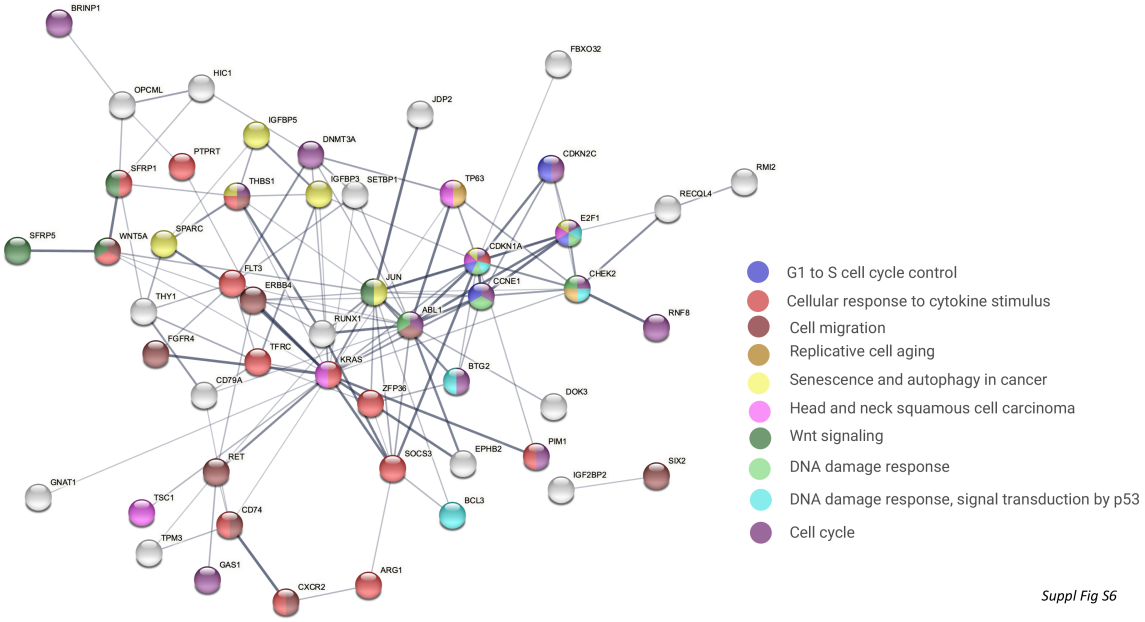

Suppl Fig S6

Supplementary Material

Materials & Methods

Quantification of immunofluorescence intensity. Red or green fluorescent signal was collected from experimental tissues in RGB format using the same exposure conditions. Regions of interest of distinct size within the epidermis or dermis were selected, and CTCF value was quantified using integrated density of the immunofluorescence against the area of selected region and mean gray value of the background. At least 10 40x-images per group with exactly the same image acquisition parameters have been taken. Statistical analysis was performed using unpaired Student's t-test; differences were deemed significant if $p<0.05$.

We used a complex approach to avoid significant errors in quantification of fluorescence intensity: i) To avoid the errors derived from the UV source, the fluorescence bulbs were regularly replaced before reaching their max lifespan by a qualified technician.

ii) To minimize the issue related to the fading of fluorescent dyes, we used Alexa-coupled secondary antibodies. Alexa dyes are proven to be more photostable than their commonly used fluorophores (N Panchuk-Voloshina et al. *Alexa dyes, a series of new fluorescent dyes that yield exceptionally bright, photostable conjugates*. J Histochem Cytochem. 1999, 47:1179-88). With maintaining the same exposure conditions that were set to avoid over- and under-saturation, an area of imaging was exposed only once for a very short time required to capture the image. Acquiring images for each immunofluorescence protocol (each antibody), including both age groups, was performed by the same person during one imaging session. Monochrome greyscale images were acquired with QIMAGING RETIGA EXI AQUA MONO camera, which supports low light fluorescent imaging, with enhanced sensitivity, high resolution, and broad spectral response (https://www.mediacy.com/support/imagepro/hardware). For illustration purpose, each greyscale

image channel was pseudo-colored and merged to produce colored images in RGB format with the Image Pro Insight 9.0 software.

iii) For image analysis, background correction for total fluorescence correction was performed. Analysis of pixel intensity values was done on raw flat-field grayscale 16-bit TIFF images that preserves the linear relationship between the photons and image intensity values.

RNA extraction and RNA-seq analyses. For RNA sequencing, approximately 10 ug of total RNA was used to remove ribosomal RNA according to the manuscript of the Epicentre Ribo-Zero Gold Kit (Illumina, San Diego, USA). Following purification, the ribo-minus RNA fractions is fragmented into small pieces using divalent cations under elevated temperature. Then the cleaved RNA fragments were reverse-transcribed to create the final cDNA library in accordance with a strand-specific library preparation by dUTP method. The average insert size for the paired-end libraries was 300±50 bp. The pair-end 2×150bp sequencing was performed on an Illumina Hiseq 4000 platform in the LC Sciences (Houston, TX).

Bioinformatics and protein-protein interaction network analyses. The bioinformatics analysis of the RNAseq data was performed by the LC Sciences (Houston, TX). Firstly, Cutadapt (Martin, 2011) and Perl scripts were used to remove the reads that contained adaptor contamination, low quality bases and undetermined bases. Then, sequence quality was verified using FastQC (http://www.bioinformatics.babraham.ac.uk/projects/fastqc/). Bowtie2 (Langmead and Salzberg, 2012) and Tophat2 (Kim et al., 2013) were used to map reads to the genome of Heterocephalus glaber (https://useast.ensembl.org/Heterocephalus_glaber_female/Info/Index). The differentially expressed mRNAs were selected with log2 (fold change) >1 or log2 (fold change) <-1 and with parametric F-test comparing nested linear models (p value < 0.05) by R package Ballgown. Ballgown was used to generate a list and heatmaps of differentially expressed genes, and in-house generated Perl scripts (LC Science, Houston, TX) were used for Gene Ontology (GO) and

Kyoto Encyclopedia of Genes and Genomes (KEGG) pathway enrichment analyses. In addition, to cluster differentially expressed genes into different functional groups, the QIAGEN Ingenuity Pathway Analysis (QIAGEN IPA) was used (https://digitalinsights.qiagen.com/products-overview/discovery-insights-portfolio/analysis-and-visualization/qiagen-ipa/) as a general platform, and skin-relevant functional gene sub-categories were manually organized accordingly to previously published data (Sharov et al., 2009, Sharov et al., 2006). Also, for each time interval, the significantly differentially expressed genes were input into HAGR (https://genomics.senescence.info/) or CGC (https://cancer.sanger.ac.uk/census) databases. In addition, ClusterProfiler R Package was used to identify KEGG Pathway enrichment and GO functional term enrichment for each of the gene sets.

To predict functional interaction of proteins encoded by differentially expressed genes in young and aged NMRs, the search tool for retrieval of interacting genes (STRING) (https://string-db.org, vision 11.0) database was employed. Active interaction sources, including text mining, experiments, databases, and co-expression as well as species limited to “Heterocephalus glaber” and an interaction score > 0.4 were applied to construct the PPI networks. GO and KEGG pathways were selected with the threshold of adjusted p-value < 0.05.

Supplementary Figure legends

Supplementary Figure S1. Characterization of young and old NMR skin

a) A quantitative analysis of active Caspase 3+ cells: no difference in expression levels between the epidermis of young and old NMRs; **b)** COL3A1 expression in the upper dermis of old NMRs: no difference in total expression levels between young and old animals; **c)** Distribution of dermal elastic fibers and Elastin expression levels are similar between the dermis of young and old animals; **d)** epidermal MMP1 expression with equal immunofluorescence intensity between young and old animals; **e)** Marked increase of MMP11 immunofluorescence in the dermis of old NMRs compared to young animals; **f)** a significant decrease in the number of CD3ε+ T-cells in the dermis of aged NMR skin; **g)** a significant decline in the number of mast cells in aged NMR skin as detected by Gimsa stain; **h)** qRT-PCR: upregulation of $p16^{INK4a}$ in aged vs young full-thickness skin samples, and similar levels of $p15^{INK4b}$ and $pALT^{INK4a/b}$ are seen in old and young skin. Mean ± SD, *p<0.01, Student's t-test. Scale bars: 25 μm. A.u. – arbitrary units, Y – young animal, O – old animal

Supplementary Figure S2. The correlation of the age-associated changes in the NMR skin transcriptome to human or mouse skin aging

Age-associated transcriptome from NMR skin was compared to the transcriptome data from aged human and mouse skin obtained from publicly available datasets (Aramillo Irizar et al. Nature Commun, 2018, 9, 327; Barth et al. Aging, 2019, 11, 8556).

a) Number of genes upregulated during aging in the NMR skin showing similarities or differences in expression in comparison to human or mouse skin aging.

b) Number of genes downregulated during aging in the NMR skin showing similarities or differences in expression in comparison to human or mouse skin aging.

Supplementary Figure S3. Validation of the changes in the NMR skin aging transcriptome by immunofluorescence

a-c) Significant increase of CDKN1A **(a)**, BTG2 (**b)** and TOB1 (**c)** immunofluorescence in the epidermis of aged NMR skin. Mean ± SD, *p<0.01, Student's t-test. A.u. – arbitrary units, Y – young animal, O – old animal. Scale bars: 25 μm.

Supplementary Figure S4. The STRING protein-protein interaction network analysis showing associations among the genes upregulated in the aged NMR skin and longevity-associated genes present in HAGR database

Color nodes represent proteins associated with the corresponding GO term and KEGG pathways, while thickness of the network edges (links) show the strength of data support used for the network reconstruction.

Supplementary Figure S5. The STRING protein-protein interaction network analysis showing associations among the genes downregulated in the aged NMR skin and longevity-associated genes present in HAGR database

Color nodes represent proteins associated with the corresponding GO term and KEGG pathways, while thickness of the network edges (links) show the strength of data support used for the network reconstruction.

Supplementary Figure S6. The STRING protein-protein interaction network analysis showing associations among the genes differentially expressed in the aged NMR skin and cancer-related/tumor suppressor genes present in CGC/TSG databases

Color nodes represent proteins associated with the corresponding GO term and KEGG pathways, while thickness of the network edges (links) show the strength of data support used for the network reconstruction.

Supplementary Tables

Supplementary Table S1. Genes Upregulated in the Skin of Old NMRs vs Young NMRs (RNAseq, FPKM, fold change)

Supplementary Table S2. Genes Downregulated in the Skin of Old NMRs vs Young NMRs (RNAseq, FPKM, fold change)

Supplementary Table S3. Correlation of the RNAseq and quantitative immunofluorescence data for selected markers expressed in young and old NMR skin

Supplementary Table S4. Expression changes of the genes upregulated in old NMR skin in the human and mouse skin during aging (RNAseq, FPKM, fold change)

Supplementary Table S5. Expression changes of the genes downregulated in old NMR skin in the human and mouse skin during aging (RNAseq, FPKM, fold change)

Supplementary Table S6. Genes up- and downregulated in the aged NMR skin and found in the Human Aging Genome Resource (HAGR) database

Supplementary Table S7. Genes up- and downregulated in the aged NMR skin and found in the Cancer Gene Census (CGC) and Tumor Suppressor Genes (TSG) databases

Supplementary Table S8. List of primary antibodies

Supplementary Table 9: List of PCR primers